

1 **A Mathematical Model for Reactions during Top-Blowing in the AOD**

2 **Process: Derivation of the Model**

3 Ville-Valtteri Visuri,^{1)*} Mika Järvinen,²⁾ Aki Kärnä,¹⁾ Petri Sulasalmi,¹⁾
4 Eetu-Pekka Heikkinen,¹⁾ Pentti Kupari³⁾ and Timo Fabritius¹⁾

5

6 1) Process Metallurgy Research Unit, University of Oulu, PO Box 4300, FI-90014 University of Oulu, Finland.

7 2) **Department of Mechanical Engineering**, Aalto University, PO Box 14440, FI-00076 Aalto, Finland.

8 3) Outokumpu Stainless Oy, FI-95490 Tornio, Finland.

9 *) Corresponding author. E-mail: ville-valtteri.visuri@oulu.fi

10 **Abstract**

11 In earlier work, a fundamental mathematical model was proposed for side-blowing operation in the
12 argon-oxygen decarburization (AOD) process. The purpose of this work is to present a new model,
13 which focuses on the reactions during top-blowing in the AOD process. The model considers
14 chemical reaction rate phenomena between the gas jet and the steel bath as well as between the gas
15 jet and metal droplets. The rate expressions were formulated according to a law of mass action based
16 method, which accounts for the mass transfer resistances in the liquid metal, gas and slag phases. The
17 generation rate of the metal droplets was related to the blowing number theory. This paper presents
18 the description of the model, while validation and preliminary results are presented in the second part
19 of this work.

20

21 **Keywords:** stainless steelmaking, AOD process, top-blowing, mathematical modelling.

22 **1 Introduction**

23 The argon-oxygen decarburization (AOD) process is the most common process for the refining of
24 stainless steel.^[1] Owing to violent agitation caused by the high blowing rates, the AOD vessel has
25 very good mixing characteristics.^[2-5] Nowadays, top-blowing is employed in conjunction with side-
26 blowing in the early part of the decarburization stage in order to maximize oxygen delivery into the
27 melt.^[6] As illustrated in **Figure 1**, two main reaction areas can be identified during combined blowing:
28 1) inside the gas plume, and 2) on the surface of the bath, including metal droplets.^[7,8]

29

30 **Figure 1**

31

32 Numerous reaction models have been proposed for the decarburization^[8-37] and nitrification^[7,38-40] of
33 steel in an AOD vessel. The majority of the models applicable for side-blowing decarburization have
34 been reviewed elsewhere^[21,41]. Despite the vast number of reaction models available, there are only
35 a few models that explicitly address the reactions during top-blowing in the AOD process. Arguably
36 the most relevant examples found in the literature are those proposed by Watanabe and Tohge^[9],
37 Tohge *et al.*^[17], Kikuchi *et al.*^[23,42] and Wei *et al.*^[8,21,22,26,28]. Some similarities in the modelling setting
38 can be found in the reaction models proposed for the VOD process^[41,43]. To summarize, it can be
39 stated that the top-blowing models proposed so far are capable of predicting the decarburization with
40 a reasonable degree of accuracy and have laid the basic foundations for further investigations.
41 However, more research is required along these lines in order to obtain information on the related
42 reaction interfaces and chemical reaction rate phenomena.

43

44 In our previous work,^[29,30] a fundamental model was proposed and validated for the reactions inside
45 the bath during side-blowing in the AOD process. Consequently, the aim of this work was to extend
46 the original model by developing a mathematical model for reactions during top-blowing. In order to
47 provide more information on the controlling mechanisms and dynamics of decarburization during
48 top-blowing, the model combines the transient solution of multicomponent equilibria with a
49 description of the constraining mass transfer. This paper presents the description of the model, while
50 validation and preliminary results are presented in the second part of this work^[44].

51

52 **2 Derivation of the model**

53 The model was programmed using C++ and its main assumptions can be summarized as follows:

54

55 1. The top-blown oxygen may react with iron and species dissolved in iron, dissolve in the steel

- 56 bath, or escape through the gas exit.
- 57 2. Reactions between gas, metal and slag species take place simultaneously at the surface of the
- 58 cavity as well as at surface of the metal droplets generated due to top-blowing.
- 59 3. Owing to the high temperature, the reaction rates are assumed to be limited by mass transfer
- 60 onto and from the reaction interfaces and hence the reaction interfaces are able to reach their
- 61 constrained thermodynamic equilibrium at any given moment.
- 62 4. Conservation of mass and heat are solved successively.

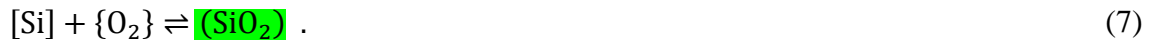
63

64 The liquid metal phase is assumed to consist of Fe as the solvent and Cr, Mn, Si, C, O, N, Ni, Al and

65 S as solutes. The gas phase consists of O₂, CO, CO₂, N₂ and Ar. The slag phase consists of FeO,

66 Cr₂O₃, MnO, SiO₂, CaO, MgO, Al₂O₃, CaF₂ and MeO_x, which is a generic oxide and depicts the

67 residual species. The reaction system considered is defined by the following reactions:



69

70 The rate expressions were formulated as reversible according to a modified Law of Mass Action, a

71 method that has been discussed more comprehensively in our earlier work^[45,46]. More specifically,

72 the rate expressions are defined so that concentrations are replaced with activities and partial

73 pressures, as illustrated below for the oxidation of dissolved carbon to carbon monoxide:

$$R'' = k_f \left(a_{[C]} p_{O_2}^{1/2} - \frac{p_{CO}}{K} \right) , \quad (8)$$

75

76 where k_f is the forward reaction rate coefficient, $a_{[C]}$ is the activity of dissolved carbon, p_{O_2} is the

77 partial pressure of gaseous oxygen and K is the equilibrium constant.

78

79 **2.1 Conservation of mass**

80 The observed system consists of gas input, gas exit, two reaction interfaces and three bulk volumes,
 81 as shown in **Figure 2**. It should be noted that the reaction interfaces have neither thickness nor mass.

82

83 **Figure 2**

84

85 It has been proposed that during simple side-blowing, post-combustion takes place in the off-gas flue,
 86 but not in the AOD vessel itself.^[47] However, during combined top- and side-blowing a part of the
 87 top-blown oxygen may be consumed in the post-combustion of CO to CO₂ before the gas jet impacts
 88 the bath surface.^[8] In order to simplify the modelling setting, the model proposed in this paper
 89 considers post-combustion only at the reaction interfaces. Because the entrainment of cold air from
 90 the atmosphere outside the vessel can be neglected under normal operating conditions,^[48] the top-
 91 lance and the tuyères can be taken as the only gas inputs of the system. More specifically, it was
 92 assumed that the side-blown gas exits the metal bath through the plume eye and becomes in contact
 93 with the top-blown gas. The mass flow of gaseous species through the top lance into the observed
 94 system is given by

95

$$\dot{m}_{G,in,lance} = \dot{V}_{G,lance} \rho_{G,STP} \quad (9)$$

96

97 where $\dot{V}_{G,lance}$ is the volumetric gas flow rate through top lance (in Nm³/s) and $\rho_{G,STP}$ is the density
 98 of the gas mixture under standard temperature and pressure according to the DIN 1343 standard^[49]:
 99 273.15 K (0 °C) and 101325 Pa. The model is coupled with the earlier-proposed model for side-
 100 blowing decarburization^[29], which calculates the mass flow of gaseous species from the plume eye (
 101 into the observed system. In the case of inert gases, the mass flow rate of gas from the plume eye is
 102 equal to the mass flow rate of gas from the tuyères. Preventing the suction of atmospheric gas, the
 103 mass flux of gas exiting the system is obtained from

104

$$\dot{m}_{G,out} = \max \left(\underbrace{\dot{m}_{G,in,lance} + \dot{m}_{G,in,plume}}_{\text{gas injection}}, \underbrace{-\dot{m}_{G,cav} - \dot{m}_{G,md}}_{\text{gas consumption}}, 0 \right), \quad (10)$$

105

106 where $\dot{m}_{G,in,plume}$ is the mass flow of gas from the plume eye, $\dot{m}_{G,cav}$ is the mass flow of gas from
 107 the cavity interface and $\dot{m}_{G,md}$ is the mass flow of gas from the metal droplet interface. In order to
 108 avoid the mathematical complexity of the Maxwell-Stefan equations and the generalized Fick's law,
 109 an effective diffusion model was employed^[50]. The conservation of species at the two reaction

110 interfaces is defined by the reaction rates and mass transfer onto and from the reaction surfaces.
 111 Employing a first-order upwind scheme for the Stefan flow, the conservation of species i in phase ψ
 112 at reaction interface ω is given by

$$\begin{aligned}
 & \underbrace{\beta_{i,\psi,\omega} \rho_{\psi,\omega} (y_{i,B} - y_{i,\omega}^*)}_{\text{mass transport}} + \underbrace{\max(m''_{\psi,\omega}, 0) y_{i,B} - \max(-m''_{\psi,\omega}, 0) y_{i,\omega}^*}_{\text{Stefan flow}} \\
 & + \underbrace{\sum_{k=1}^r R''_{k,\omega} \bar{v}_{i,k}}_{\text{chemical reactions}} = 0, \tag{11}
 \end{aligned}$$

114
 115 where β is the mass transfer coefficient, ρ is the density, $y_{i,B}$ is the mass fraction of species i in the
 116 bulk phase (*i.e.* steel bath, gas jet or top slag), $y_{i,\omega}^*$ is the interfacial mass fraction of species i , m'' is
 117 the total mass flux, R'' is the reaction rate and \bar{v} is the mass-based stoichiometric coefficient. It should
 118 be noted that all properties are specific to the reaction interface in question. In order to account for
 119 conservation of mass within the metal droplets, the following expression is employed for species in
 120 the metal phase at the metal droplet interface:

$$\begin{aligned}
 & \underbrace{\left(\frac{m_{\text{md}}}{A_{\text{md}} \bar{t}_{\text{md}}} - m''_{L,\text{md}} \right) \bar{\eta}_{i,M,\text{md}} (y_{i,\text{bath}} - y_{i,\text{md}}^*)}_{\text{mass transport}} \\
 & + \underbrace{m''_{L,\text{md}} y_{i,\text{bath}}}_{\text{Stefan flow}} + \underbrace{\sum_{k=1}^r R''_{k,\text{md}} \bar{v}_{i,k}}_{\text{chemical reactions}} = 0, \tag{12}
 \end{aligned}$$

122
 123 where m_{md} , A_{md} and \bar{t}_{md} are the mass, surface area and average residence time of the metal droplets,
 124 respectively, and $\bar{\eta}_{i,M,\text{md}}$ is the average microkinetic efficiency for mass transfer of species i in the
 125 metal droplets. The total mass flux of the metal phase is subject to constraint $m''_{L,\text{md}} \leq \frac{m_{\text{md}}}{A_{\text{md}} \bar{t}_{\text{md}}}$. The
 126 average microkinetic efficiency was calculated based on the average residence time of the metal
 127 droplets:

$$\bar{\eta}_{i,M,\text{md}} = \frac{y_{i,\text{bath}} - y_{i,\text{md}}}{y_{i,\text{bath}} - y_{i,\text{md}}^*} = 1 - \exp\left(-\beta_{i,L,\text{md}} \frac{A_{\text{md}}}{V_{\text{md}}} \bar{t}_{\text{md}}\right), \tag{13}$$

129
 130 where $y_{i,\text{md}}$ is the composition of species i in the metal droplets. The mass-based stoichiometric
 131 coefficients $\bar{v}_{i,k}$ are defined in relation to key components:

132

$$\bar{v}_{i,k} = v_{i,k} \frac{M_i}{M_{K,k}}, \quad (14)$$

133

134 where $v_{i,k}$ is the stoichiometric coefficient of species i in reaction k , $M_{K,k}$ is the molar mass of the
 135 key component of reaction k and M_i is the molar mass of species i . The key components of the
 136 reactions shown in Eqs. 1–7 are O₂, C, C, Fe, Cr, Mn and Si, respectively. The total mass flux of
 137 phase ψ at reaction interface ω is given by:

138

$$m''_{\psi,\omega} = - \sum_{i=1}^n \sum_{k=1}^r \Gamma_{i,\psi} R''_{k,\omega} \bar{v}_{i,k}, \quad (15)$$

139

140 where $\Gamma_{i,\psi}$ is a binary operator, which is defined as 1 if species i is in phase ψ and 0 otherwise. The
 141 total mass flows $\dot{m}_{\psi,\omega}$ are obtained by multiplying the mass flux $m''_{\psi,\omega}$ by the corresponding
 142 interfacial area A_{ω} . Employing the implicit Euler method for time integration, the conservation of
 143 species i in the steel bath, top-blown gas and top slag is defined by Eqs. 16, 17 and 18, respectively.

144

$$\begin{aligned} & -\beta_{i,L,cav} \rho_{L,cav} A_{cav} (y_{i,bath} - y_{i,cav}^*) - \max(m''_{L,cav}, 0) A_{cav} y_{i,bath} \\ & + \max(-m''_{L,cav}, 0) A_{cav} y_{i,cav}^* \\ & - \left(\frac{m_{md}}{\bar{t}_{md}} - m''_{L,md} A_{md} \right) \bar{\eta}_{i,M,md} (y_{i,bath} - y_{i,md}^*) \end{aligned} \quad (16)$$

$$-m''_{L,md} A_{md} y_{i,bath} - \frac{m_{bath} y_{i,bath} - m_{bath}^{t-\Delta t} y_{i,bath}^{t-\Delta t}}{\Delta t} = 0,$$

$$\begin{aligned} & \sum_{\omega} [-\beta_{i,G,\omega} \rho_{G,\omega} A_{\omega} (y_{i,jet} - y_{i,\omega}^*) - \max(m''_{G,\omega}, 0) A_{\omega} y_{i,jet} \\ & + \max(-m''_{G,\omega}, 0) A_{\omega} y_{i,\omega}^*] + \dot{m}_{G,in,lance} y_{i,in,lance} + \dot{m}_{G,in,plume} y_{i,in,plume} \\ & - \dot{m}_{G,out} y_{i,jet} - \frac{m_{jet} y_{i,jet} - m_{jet}^{t-\Delta t} y_{i,jet}^{t-\Delta t}}{\Delta t} = 0, \end{aligned} \quad (17)$$

$$\begin{aligned} & \sum_{\omega} [-\beta_{i,S,\omega} \rho_{S,\omega} A_{\omega} (y_{i,slag} - y_{i,\omega}^*) - \max(m''_{S,\omega}, 0) A_{\omega} y_{i,slag} \\ & + \max(-m''_{S,\omega}, 0) A_{\omega} y_{i,\omega}^*] - \frac{m_{slag} y_{i,slag} - m_{slag}^{t-\Delta t} y_{i,slag}^{t-\Delta t}}{\Delta t} = 0, \end{aligned} \quad (18)$$

145

146 where m_{bath} , m_{jet} and m_{slag} are the masses of the steel bath, gas jet and top slag, respectively, and
 147 Δt is the time step. The conservation equations for the total mass of the bulk phases (for the steel

148 bath, gas jet and top slag) are defined correspondingly by summation of the mass transport terms and
 149 fluxes of species that are relevant to the bulk phase in question. Metal losses to dust were not
 150 accounted for as their effect on the composition of the steel bath is negligible.

151 2.2 Conservation of heat

152 Temperature increase is defined by the difference in heat generation and heat losses. While heat is
 153 generated by exothermic reactions, it is consumed by endothermic reactions as well as heat losses
 154 through the refractory lining, and top slag and exiting gas. The conservation of heat at the cavity
 155 interface is defined according to

$$\begin{aligned}
 & \underbrace{\alpha_{L,cav}(T_{bath} - T_{cav}^*) + \alpha_{G,cav}(T_{jet} - T_{cav}^*) + \alpha_{S,cav}(T_{slag} - T_{cav}^*)}_{\text{heat transport}} \\
 & - \underbrace{\sum_{k=1}^r R''_{k,cav} \Delta h_k}_{\text{chemical reactions}} = 0, \tag{19}
 \end{aligned}$$

157
 158 where α is the heat transfer coefficient, T_{bath} is the temperature of the steel bath, T_{cav}^* is the
 159 temperature of the cavity reaction interface, T_{jet} is the temperature of the gas jet and Δh_k is the
 160 specific reaction enthalpy of reaction k . The conservation of heat at the metal droplet interface was
 161 defined according to

$$\begin{aligned}
 & \underbrace{\frac{m_{md}}{A_{md} \bar{t}_{md}} c_{p,L} \bar{\eta}_{H,md} (T_{bath} - T_{md}^*) + \alpha_{G,md} (T_{jet} - T_{md}^*) + \alpha_{S,md} (T_{slag} - T_{md}^*)}_{\text{heat transport}} \\
 & - \underbrace{\sum_{k=1}^r R''_{k,md} \Delta h_k}_{\text{chemical reactions}} = 0 \tag{20}
 \end{aligned}$$

163
 164 where T_{md}^* is the interfacial temperature of the metal droplets and $\bar{\eta}_{H,md}$ is the average microkinetic
 165 efficiency of heat transfer in the metal droplets:

$$\bar{\eta}_{H,md} = \frac{T_{bath} - T_{md}}{T_{bath} - T_{md}^*} = 1 - \exp\left(-\alpha_{L,md} \frac{A_{md}}{m_{md} c_{p,L}} \bar{t}_{md}\right), \tag{21}$$

167
 168 where T_{md} is the temperature of the metal droplets. Employing the implicit Euler method for time
 169 integration, the conservation of heat in the steel bath, in the top-blown gas and in the top slag can be

170 expressed according to Eqs. 22, 23 and 24, respectively.

171

$$\begin{aligned}
 & -\alpha_{L,cav} A_{cav} (T_{bath} - T_{cav}^*) - \frac{m_{md}}{t_{md}} c_{p,L} \bar{\eta}_{H,md} (T_{bath} - T_{md}^*) \\
 & - \sum_{\omega} \sum_{i=1}^n \sum_{k=1}^r \Gamma_{i,L} R''_{k,\omega} \bar{v}_{i,k} A_{\omega} c_{p,i} (T_{bath} - T_{\omega}^*) - q_{lining} A_{lining}
 \end{aligned} \tag{22}$$

$$\begin{aligned}
 & - m_{bath} c_{p,bath} \frac{T_{bath} - T_{bath}^{t-\Delta t}}{\Delta t} = 0, \\
 & \sum_{\omega} \left[-\alpha_{G,\omega} A_{\omega} (T_{jet} - T_{\omega}^*) - \sum_{i=1}^n \sum_{k=1}^r \Gamma_{i,G} R''_{k,\omega} \bar{v}_{i,k} A_{\omega} c_{p,i} (T_{jet} - T_{\omega}^*) \right] \\
 & - \dot{m}_{G,in,lance} \int_{T_{in}}^{T_{jet}} c_{p,lance} dT - \dot{m}_{G,in,plume} \int_{T_{plume}}^{T_{jet}} c_{p,plume} dT
 \end{aligned} \tag{23}$$

$$\begin{aligned}
 & - m_{jet} c_{p,jet} \frac{T_{jet} - T_{jet}^{t-\Delta t}}{\Delta t} = 0, \\
 & \sum_{\omega} \left[-\alpha_{S,\omega} A_{\omega} (T_{slag} - T_{\omega}^*) - \sum_{i=1}^n \sum_{k=1}^r \Gamma_{i,S} R''_{k,\omega} \bar{v}_{i,k} A_{\omega} c_{p,i} (T_{slag} - T_{\omega}^*) \right] \\
 & - q_{slag} A_{slag} - m_{slag} c_{p,slag} \frac{T_{slag} - T_{slag}^{t-\Delta t}}{\Delta t} = 0,
 \end{aligned} \tag{24}$$

172

173 where q_{lining} is the heat flux through the refractory lining, A_{lining} is the surface area of the refractory
 174 lining, q_{slag} is the heat flux through the slag and A_{slag} is the cross-sectional surface area of the top
 175 slag. The values of A_{lining} and A_{slag} are calculated based on the geometry of the simulated converter.
 176 The heat flux through the refractory lining was set to $q_{lining} = 12500 \text{ W/m}^2$ as in our previous work^[29].

177 The heat losses through the slag were determined on the basis of radiative heat transfer through the
 178 mouth of the vessel. Neglecting back-radiation, the radiative heat flux can be calculated as follows:^[51]

179

$$q_{slag} = \frac{\sigma T_{slag}^4}{\left[\frac{A_{slag} + A_{mouth} - 2A_{slag}F}{A_{mouth} - A_{slag}F^2} + \left(\frac{1}{\varepsilon_S} - 1 \right) \right]}, \tag{25}$$

180

181 where σ is the Stefan-Boltzmann constant, F is the view factor between the top slag and the converter
 182 mouth, A_{mouth} is the cross-sectional area of the vessel mouth and ε_S is the emissivity of the slag
 183 phase, which was assumed to be $\varepsilon_S = 0.95$. The view factor for the top slag in relation to the vessel
 184 mouth is determined by^[51]

185

$$F = \frac{1}{2r_{\text{slag}}^2} \left[z^2 + r_{\text{slag}}^2 + r_{\text{mouth}}^2 - \left\{ (z^2 + r_{\text{slag}}^2 + r_{\text{mouth}}^2)^2 - 4r_{\text{slag}}^2 r_{\text{mouth}}^2 \right\}^{1/2} \right], \quad (26)$$

186

187 where z is the distance between the top slag and the vessel mouth, r_{slag} is the radius of the top slag
 188 and r_{mouth} is the radius of the vessel mouth. The cooling effect of the side-blown gas on the steel
 189 bath temperature is calculated separately by the earlier-proposed model for side-blowing
 190 decarburization^[29] and is not repeated here.

191 2.3 Geometry of the cavity

192 The gas jet exits the lance nozzle at a supersonic velocity, but starts to spread and lose its velocity
 193 after the supersonic core. The entrainment of gases from the ambient atmosphere affects the gas jet
 194 not only by decreasing its velocity, but also by increasing its mass flow and – if the ambient
 195 temperature is higher than that of the gas jet – by increasing its temperature.^[52] Considering that the
 196 length of the supersonic region is typically 20–30 times the nozzle exit diameter at steelmaking
 197 temperatures^[53] it is apparent that the gas jet impacts the surface of the steel bath at subsonic velocity.
 198 Upon impact, the momentum of the gas jet forms a cavity on the bath surface,^[53] while the liquid steel
 199 outside the cavity is pushed towards the refractory walls of the vessel in the radial direction^[5].

200

201 Molloy^[54] distinguished three cavity modes, namely *dimpling*, *splashing* and *penetrating*. Dimpling
 202 refers to mere depression of the surface without droplet formation, while outwardly directed splashes
 203 start to form the edges of the depression when the mode changes to splashing. In the penetrating
 204 mode, the penetration depth is deeper and outwardly directed splashes are reduced. The different
 205 modes can also be distinguished based on the frequency and amplitude of the cavity oscillation.^[55]
 206 **Figure 3** presents a schematic illustration of the gas jet impact area with a one-hole lance in the
 207 splashing mode.

208

209 **Figure 3**

210

211 In this work, the modelling setting was simplified by defining the reaction area between the gas jet
 212 and the steel bath as the surface area of the cavity. Because the surface of the cavity is in oscillating
 213 motion, the analysis must be based on quasi-steady state flow conditions.^[53,56] It has been suggested
 214 that chemical reactions^[57,58] and the interference of top slag^[57] do not affect the geometry of the cavity
 215 to a significant extent and on this account their effect was excluded in this work. In accordance with
 216 Cheslak *et al.*^[59], it was assumed that the geometry of the cavity follows the form of a paraboloid of
 217 revolution with an impact radius of r_{cav} and an impinging depth of h_{cav} (see **Figure 3**). The surface

218 area of the paraboloid of revolution, excluding its base, can be calculated as follows:^[60]

219

$$A_{\text{cav},1} = \frac{\pi r_{\text{cav}}}{6 h_{\text{cav}}^2} [(r_{\text{cav}}^2 + 4h_{\text{cav}}^2)^{3/2} - r_{\text{cav}}^3]. \quad (27)$$

220

221 For a three-hole lance, the geometry is slightly more complicated. Depending on the inclination angle
222 of the gas jets, the gas jets may either coalesce and form only one large cavity, or penetrate the bath
223 surface as three separate jets, whereupon each gas jet will form its own cavity.^[61,62] Even if the gas
224 jets do not coalesce, the cavities may still coalesce provided that they are sufficiently close to each
225 other^[63] as shown in **Figure 4**. Observations with high-speed cameras^[64] suggest that the cavities
226 remain non-coalescing when the inclination angle is greater than 10°. In this work, it is assumed that
227 the gas jets do not coalesce and that the number of cavities is equal to the number of the gas jets (see
228 **Figure 4A**). Therefore, the total surface area of the cavities caused by a multi-hole lance can be
229 calculated simply by multiplying the surface area of a single cavity with the number of exit ports in
230 the top lance.^[52,65]

231

$$A_{\text{cav}} = n_{\text{lance}} \times A_{\text{cav},1}. \quad (28)$$

232

233 **Figure 4**

234

235 The effects of various factors on the depth and form of the cavity have been studied extensively. In
236 this work, the correlations for the geometry of the cavity were taken from Koria and Lange^[63]. The
237 equations required for calculating the depth and radius of the cavity are given in **Table 1**. These are
238 based on a dimensional analysis of experimental data on the penetration of oxygen jets in molten pig
239 iron and pure iron-carbon alloys with both single- and multi-hole lances.^[63] **It should be noted that**
240 **Eq. 35 is applicable only for diatomic ideal gases (e.g. O₂ or N₂) and their mixtures. For other gas**
241 **mixtures, a more general expression for \dot{m}_t can be derived based on the equations presented by**
242 **Koria^[66].**

243

244 **Table 1** Ref.^[63]

245 Eq. (29)

246 Eq. (30)

247 Eq. (31)

248 Eq. (32)

249 Eq. (33)

250 Eq. (34)

251 Eq. (35)

252

253 2.4 Droplet generation

254 The generation of metal droplets during top-blowing is important for steelmaking processes, because
255 it brings about a considerable increase in the interfacial area available to chemical reactions.^[67] The
256 contribution of metal droplets to the decarburization rate during top-blowing in the AOD process has
257 been acknowledged likewise^[7,8,23,42,68–70]. However, foaming of the AOD slag does take place under
258 typical operating conditions. Considering the high blowing rates and high viscosity of the slag, the
259 behavior of slag should be somewhere between a void-free and an expanded slag. In such case the
260 gas void fraction would depend on the gas velocity.^[71]

261
262 Different mechanisms contribute to generation of metal droplets. If the momentum flux of the top-
263 blown gas jet is sufficiently high, the liquid surface becomes unstable and the splashing of metal
264 droplets occurs.^[72] Standish and He^[73] identified two regions of droplet generation: *dropping* and
265 *swarming*. In the dropping region, single droplets are gradually formed and ejected. This is the
266 mechanism of droplet generation when the gas flow rate is relatively low. When the gas flow rate is
267 increased past a certain limit, the system reaches the swarming region and the mechanism of droplet
268 generation changes so that not only single droplets but also large tears of liquid phase are ejected
269 from the bath. Formation of metal droplets is also caused by side-blowing through a mechanism
270 referred to as bubble bursting.^[74–77] This phenomenon occurs when a rising gas bubble reaches the
271 surface of the steel and bursts creating very small metal droplets from the thin film of steel around
272 the bubble.^[74–77] A related mechanism is the entrainment of large droplets due to jet formation, which
273 is caused by the collapsing of the cavity after the rupture of the iron film.^[76]

274
275 The secondary break-up of the metal droplets can occur due to various reasons, *e.g.* due to the
276 aerodynamic forces of the gas jet^[78], impact on the slag layer^[79] or bursting resulting from
277 spontaneous CO nucleation within the droplet^[80]. In the absence of suitable quantitative descriptions
278 for the break-up mechanisms and due to uncertainties related to the trajectories of the droplets, the
279 effect of the various break-up mechanisms on the droplet size distribution was not accounted for.

280
281 Based on the available knowledge, the lifespan of the metal droplets was assumed to consist of three
282 successive steps. At first, the metal droplets are generated at the vicinity of the cavity, from which
283 they are ejected onto a gas–metal–slag emulsion. This also includes metal droplets, which have been
284 ejected into the atmosphere and land on the emulsion. Thereafter, the metal droplets pass through the
285 emulsion layer, reacting simultaneously with gas and slag species. Finally, the metal droplets return
286 to the steel bath, where they mix with the steel bath immediately. Based on experimental findings^[81]
287 it was assumed that the initial composition of the metal droplets corresponds to the bulk composition.

288 Furthermore, the metal droplets were assumed to be spherical in geometry. This assumption should
 289 hold well for small droplets,^[82] which are expected to form the majority of the surface area.
 290 Considering the distribution of emulsified metal droplets residing in the emulsion, their mass and
 291 surface area are obtained from the following equations:

$$m_{\text{md}} = \sum_i m_{\text{md},i}, \quad (36)$$

$$A_{\text{md}} = \sum_i \frac{6m_{\text{md},i}}{d_{\text{md},i}\rho_L}, \quad (37)$$

293
 294 where $m_{\text{md},i}$ and $d_{\text{md},i}$ are the mass and diameter of the droplet size class i , respectively. As a
 295 practical matter, the droplet distribution was calculated from a diameter of 0.1 mm up to the diameter
 296 corresponding to the largest 99.9% by weight using a step size of 0.1 mm. The mass of droplets in
 297 the size class i residing in the emulsion can be solved from

$$m_{\text{md},i} = f_{\text{md},i} \dot{m}_{\text{md}} \min(t_{\text{md},i}, t), \quad (38)$$

298
 299 where $f_{\text{md},i}$, \dot{m}_{md} and $t_{\text{md},i}$ are the mass fraction of size class i at place of birth, the metal droplet
 300 generation rate and the residence time of size class i , respectively, and t is the time. The Sauter mean
 301 diameter of the metal droplets residing in the emulsion at a given moment is obtained from
 302
 303

$$d_{32,\text{md}} = \frac{6m_{\text{md}}}{\rho_L A_{\text{md}}}. \quad (39)$$

304 2.4.1 Droplet generation rate

305 The blowing number, which relates the intensity of the jet momentum to the properties of the liquid
 306 steel, is defined by^[67]

$$N_B = \frac{\rho_G u_G^2}{2\sqrt{\sigma_L g \rho_L}} = \frac{\eta^2 p_d}{\sqrt{\sigma_L g \rho_L}} \quad \text{where} \quad \eta = \frac{u_G}{u_j}, \quad (40)$$

308
 309 where u_G denotes the critical gas velocity, σ_L is the surface tension of the steel, η is a constant, p_d is
 310 the dynamic pressure of the gas jet and u_j is the axial velocity of the gas jet. The criterion for the
 311 Kelvin–Helmholtz instability, and thus the onset of droplet formation, is represented with a value of
 312 $N_B = 1$.^[67] The experimental results of other studies suggest that η is not independent of the lance

313 height^[83–85] or the gas jet angle^[86]. Here, the variation of η as a function of the gas jet angle was
 314 treated in a similar fashion as by Alam *et al.*^[86]. Making use of the concept of blowing number,
 315 Subagyo *et al.*^[67] proposed an empirical expression for droplet generation rate (\dot{m}_{md}) in the splashing
 316 cavity mode:

$$\frac{\dot{m}_{md}}{\dot{V}_{G,lance}} = \frac{(N_B)^{3.2}}{[2.6 \times 10^6 + 2.0 \times 10^{-4}(N_B)^{12}]^{0.2}} \quad R^2 = 0.97, \quad (41)$$

318
 319 where $\dot{V}_{G,lance}$ is the volumetric gas flow rate through the top lance (Nm³/s). As noted by Sarkar *et al.*^[87]
 320 and Rout *et al.*^[88], Eq. 41 yields droplet generation rates which are considerably below the
 321 values estimated from plant data. According to Rout *et al.*^[88], one reason for the discrepancy is the
 322 fact that Eq. 41 has been derived for conditions corresponding to room temperature. Similar to Rout
 323 *et al.*^[88], Eq. 41 was modified such that the blowing number N_B and the volumetric gas flow rate
 324 $\dot{V}_{G,lance}$ are temperature corrected for the conditions at the point of impact:

$$\frac{\dot{m}_{md}}{\dot{V}'_{G,lance}} = \frac{(N'_B)^{3.2}}{[2.6 \times 10^6 + 2.0 \times 10^{-4}(N'_B)^{12}]^{0.2}}, \quad (42)$$

326
 327 where N'_B is the modified blowing number and $\dot{V}'_{G,lance}$ is the modified volumetric gas flow rate. The
 328 modified blowing number N'_B is obtained from Eq. 40 by employing the dynamic pressure at the point
 329 of impact. In this work, the dynamic pressure at the point of impact was calculated according to an
 330 experimental relationship proposed by Deo and Boom^[52]:

$$p_d = 230 p_0 \left(\frac{h_{lance}}{d_t} \right). \quad (43)$$

332
 333 The modified gas flow rate is calculated as follows:^[88]

$$\dot{V}'_{G,lance} = \frac{p_{G,STP}}{p_G} \frac{T_G}{T_{G,STP}} \dot{V}_{G,lance}, \quad (44)$$

335
 336 where $p_{G,STP}$ is the standard pressure, p_G is the total pressure of the gas at the impact point, T_G is the
 337 temperature of the gas at the impact point and $T_{G,STP}$ is the standard temperature. Rout *et al.*^[88]
 338 suggested also that due to low lance height, the experiments conducted by Subagyo *et al.*^[67] did not
 339 actually correspond to splashing mode, but rather the penetrating mode of jet interaction, which is

340 characterized by a lower droplet generation rate than the splashing mode. For this reason, a
 341 dimensionless parameter J_{eff} was introduced similar to Sarkar *et al.*^[87] in order to calculate the
 342 effective droplet generation rate:

$$\dot{m}_{\text{md,eff}} = J_{\text{eff}} \times \dot{m}_{\text{md}}. \quad (45)$$

344
 345 It should be noted that J_{eff} is essentially a fitting parameter, which is evaluated based on plant data.

346 2.4.2 Droplet size distribution

347 The size distribution of the metal droplets at their place of birth was determined according to Koria
 348 and Lange^[89], who proposed a formulation based on the Rosin-Rammler-Sperling (RRS) function:

$$RF = (0.001) \left(\frac{d_{\text{md},i}}{d_{\text{limit}}} \right)^n, \quad (46)$$

350
 351 where RF is the cumulative weight-fraction, d_{limit} is the limiting droplet diameter (which
 352 corresponds to $RF = 0.001$) and n is the distribution exponent. Experimental studies indicate that the
 353 parameter n is independent from the limiting diameter^[89], maximum impact pressure of the gas jet^[89]
 354 and the blowing number^[67]. The reported values for the parameter n vary in a relatively wide range
 355 from 1.0 to 1.828.^[89,90] In this work, a value of $n = 1.26$ was taken from Koria and Lange^[89], because
 356 it represents an arithmetic mean for a relatively large amount of data. For non-coalescing jets, the
 357 limiting diameter (in m) can be obtained from^[91]

$$d_{\text{limit}} = 5.513 \times 10^{-6} \times \left[10 \left(\frac{d_{\text{t}}^2}{h_{\text{lance}}^2} \right) p_{\text{amb}} \left(1.27 \frac{p_0}{p_{\text{amb}}} - 1 \right) \cos \theta \right]^{1.206}, \quad (47)$$

359
 360 where p_0 and p_{amb} are the lance supply pressure (in Pa) and the ambient pressure (in Pa),
 361 respectively. This expression suggests that droplet sizes increase with increasing lance supply
 362 pressure and decreasing lance height, and thus it appears to be in accordance with other studies^[67,90,92].
 363 Modifying the expression presented by Deo *et al.*^[93] to a more general form, the mass fraction of size
 364 class i at place of birth can be obtained from

$$f_{\text{md},i} = -\ln(0.001) n RF \frac{d_{\text{md},i}^{n-1}}{d_{\text{limit}}^n}. \quad (48)$$

366 **2.4.1 Residence time**

367 The average residence time of the metal droplets is obtained from

368

$$\bar{t}_{\text{md}} = \frac{m_{\text{md}}}{\dot{m}_{\text{md}}}. \quad (49)$$

369

370 According to the results available in the literature, the average residence time of the droplets increases
 371 with an increasing top gas flow rate^[94] and decreasing droplet size^[94,95]. As shown by Urquhart and
 372 Davenport^[96], the size distribution of the metal droplets in the emulsion is shifted towards smaller
 373 droplets than the distribution of the generated droplets. The residence time of an individual droplet in
 374 the emulsion can be defined as the ratio of the trajectory length to the average velocity.^[67] However,
 375 for the simplified setting considered in this work, it is more convenient to define the residence time
 376 of size class i through a constant κ as follows:^[67]

377

$$t_{\text{md},i} = \kappa \frac{h_{\text{em}}}{u_{\text{md},i}}, \quad (50)$$

378

379 where h_{em} is the height of the emulsion layer and $u_{\text{md},i}$ is the terminal velocity of size class i .
 380 Because the residence time approaches infinity as the droplet diameter approaches zero, the residence
 381 time was limited to $t_{\text{md},i} \leq 60$ s in order to avoid computational problems. The terminal velocity of
 382 the metal droplets in the emulsion was defined in three Reynolds ranges according to the equations
 383 proposed by Subagyo and Brooks^[97]. In the absence of suitable values, κ was taken here as unity.
 384 Moreover, it was assumed that all droplets of the same size class have the same residence time. The
 385 average thickness of the emulsion layer can be approximated from:

386

$$h_{\text{em}} = \frac{m_{\text{em}}}{A_{\text{slag}}\rho_{\text{em}}} = \frac{m_{\text{em}}}{(A_{\text{bath}} - n_{\text{lance}} \times \pi r_{\text{cav}}^2)\rho_{\text{em}}}, \quad (51)$$

387

388 where m_{em} is the mass of the emulsion, A_{slag} is the surface area of the top slag layer residing around
 389 the cavities, ρ_{em} is the density of the emulsion and A_{bath} is the cross-sectional area of the steel bath.
 390 The density of the slag-metal-slag emulsion is calculated according to:^[97]

391

$$\rho_{\text{em}} = \rho_{\text{L}}\phi_{\text{L}} + \rho_{\text{S}}(1 - \phi_{\text{L}}), \quad (52)$$

392

393 where ϕ_{L} denotes the volume fraction of metal droplets in emulsion, and is obtained from

394

$$\phi_L = \frac{V_L}{V_L + V_G + V_S} \quad \text{where} \quad V_G = \frac{\phi_G}{1 - \phi_G} (V_L + V_S), \quad (53)$$

395

396 where V_L , V_G and V_S denote the volumes of metal, gas and slag phases in emulsion, respectively. The
397 volume-fraction of gas in the emulsion was solved numerically from the correlation proposed by Gou
398 *et al.*^[98];

399

$$\frac{\phi_G^2}{1 - \phi_G} = 0.91 u_s^{0.57}, \quad (54)$$

400

401 where u_s is the superficial velocity. The superficial velocity was defined as the ratio of gas flow rate
402 from the plume and cross sectional area of the slag layer, *i.e.* $u_s = \dot{V}_{G,\text{plume}}/A_{\text{slag}}$.

403 2.5 Mass and heat transfer coefficients

404 The mass and heat transfer coefficients were defined according to Eqs. 55 and 56, respectively.

405

$$\beta = \text{Sh} \frac{D}{L}, \quad (55)$$

$$\alpha = \text{Nu} \frac{\lambda}{L}, \quad (56)$$

406

407 where Sh is the Sherwood number, D is the mass diffusivity, L is the characteristic length, Nu is the
408 Nusselt number and λ is the heat conductivity. A detailed treatment of these parameters is provided
409 in the following subsections.

410 2.5.1 Cavity interface

411 At the cavity interface, the cavity radius (r_{cav}) was employed as the characteristic length. The mass
412 transfer correlations employed for the gas jet were taken from Oeters^[99]. These correlations are based
413 on the experimental data published by Lohe^[100] and can be represented as follows:

414

$$\text{Sh} = \begin{cases} 1.41 \text{Re}^{0.51} \text{Sc}^{0.33} & \text{when } 2 \times 10^3 \leq \text{Re} \leq 3 \times 10^4 \\ 0.41 \text{Re}^{0.75} \text{Sc}^{0.33} & \text{when } 3 \times 10^4 \leq \text{Re} \leq 2 \times 10^5 \end{cases}, \quad (57)$$

415

416 where Re is the Reynolds number and Sc is the Schmidt number. Similarly to Dogan *et al.*^[101], the

417 values of Re and Sc were defined in relation to the properties of the gas film at the impact surface:

418

$$\text{Re} = \frac{u_G r_{\text{cav}} \rho_G}{\mu_G}, \quad (58)$$

$$\text{Sc} = \frac{\mu_G}{\rho_G D_G}, \quad (59)$$

419

420 where u_G is the critical gas velocity, μ_G is the dynamic viscosity of the gas film and ρ_G is the density
421 of the gas film. The critical gas velocity (u_G) is calculated from the free axial velocity of the gas jet

422 (u_j). For the metal phase in contact with gas jet, the turbulent diffusion boundary layer thickness and
423 the corresponding Sherwood number were defined according to Eqs. 60 and 61, respectively.^[99]

424

$$\delta_N = \sqrt{\frac{D_L \sigma_{\text{equiv}}}{0.41 \rho_L u_\tau^3}}, \quad (60)$$

$$\text{Sh} = \frac{r_{\text{cav}}}{2\delta_N}, \quad (61)$$

425

426 where u_τ is the turbulent shear stress velocity and σ_{equiv} is the equivalent surface tension. The
427 thickness of the thermal boundary layer (δ_{Pr}) can be obtained from Eq. 60 by replacing the mass
428 diffusivity D_L with the ratio μ_L/ρ_L , i.e. kinematic viscosity. As a first approximation, the mass
429 transfer coefficients of the slag species were calculated similarly to the metal species, but using the
430 properties of the slag species. Similar to Memoli *et al.*^[102], the turbulent shear stress velocity was
431 calculated on the basis of momentum transfer between the gas jet and the metal bath. Assuming that
432 the axial velocity of the gas jet is zero at the bottom of the cavity, the turbulent shear stress velocity
433 can be calculated as follows:

434

$$u_\tau = \sqrt{\frac{\rho_G}{\rho_L}} u_j. \quad (62)$$

435 The heat transfer coefficients for gas, metal and slag phases were derived from the mass transfer
436 correlations according to the analogue of heat and mass transfer by replacing the Sherwood number
437 (Sh) and the Schmidt number (Sc) with the Nusselt number (Nu) and the Prandtl number (Pr),
438 respectively.

439 2.5.2 Metal droplet interface

440 At the metal droplet interface, the mass and heat transfer coefficients were calculated by employing
 441 the Sauter mean diameter of the metal droplets ($d_{32,md}$) as the characteristic length. The mass transfer
 442 coefficient mass of the gas phase in contact with the metal droplets can be calculated from the
 443 Steinberger and Treybal^[103] correlation, which accounts for the effects of both natural and forced
 444 convection:

$$Sh = Sh_0 + 0.347(ReSc^{1/2})^{0.62}, \quad (63)$$

$$Sh_0 = \begin{cases} 2 + 0.569(\overline{Gr}Sc)^{1/4} & \text{for } \overline{Gr}Sc < 10^8 \\ 2 + 0.0254(\overline{Gr}Sc)^{1/2} Sc^{0.244} & \text{for } \overline{Gr}Sc > 10^8 \end{cases}, \quad (64)$$

446
 447 where \overline{Gr} is the mean Grashof number. The mean Grashof number (\overline{Gr}), the Reynolds number (Re)
 448 and the Schmidt number (Sc) were defined as follows:

$$\overline{Gr} = Gr_M + Gr_H \left(\frac{Sc}{Pr} \right)^{1/2}, \quad (65)$$

$$Re = \frac{u_G d_{32,md} \rho_G}{\mu_G}, \quad (66)$$

$$Sc = \frac{\mu_G}{\rho_G D_G}, \quad (67)$$

450 where Gr_M is the Grashof number for mass transfer, Gr_H is the Grashof number for heat transfer and
 451 Pr is the Prandtl number. Here, Gr_M , Gr_H and Pr were defined according to Eqs. 68, 69 and 70,
 452 respectively. It should be noted that the value of Gr_M depends on the species in question.

$$Gr_{M,i} = \frac{g \rho_G d_{32,md}^3 (y_{i,md}^* \rho_{G,md} - y_{i,jet} \rho_{G,jet})}{\mu_G^2}, \quad (68)$$

$$Gr_H = \frac{g \rho_G^2 d_{32,md}^3 (T_{md}^* - T_{jet})}{T_G \mu_G^2}, \quad (69)$$

$$Pr = \frac{c_{p,G} \mu_G}{\lambda_G}, \quad (70)$$

454
 455 where $c_{p,G}$ is the specific heat capacity of the gas phase and λ_G is the heat conductivity of the gas
 456 phase. The heat transfer coefficient was calculated with the help of Eqs. 63 and 64 by replacing Sh,

457 \overline{Gr} and Sc with Nu , Gr_H and Pr , respectively. It is known that mass transfer within small metal
 458 droplets takes place almost entirely by diffusion, while larger droplets may exhibit uninhibited
 459 circulatory flow.^[99,104] In this work, it was assumed that only creeping laminar circulation takes place
 460 within the metal droplets. Therefore, the mass transfer coefficient can be calculated according to the
 461 Kronig and Brink^[105] solution, which can be expressed in terms of the Sherwood number as
 462 follows:^[106]

$$Sh = \frac{32 \sum_{i=1}^{\infty} A_i^2 \lambda_i \exp(-16\lambda_i Fo_M)}{3 \sum_{i=1}^{\infty} A_i^2 \exp(-16\lambda_i Fo_M)}, \quad (71)$$

464
 465 where Fo_M is the Fourier number for mass transfer. The first seven values for the parameters A_i and
 466 λ_i were taken from the literature^[107] and provide a sufficient convergence. **Despite its limited range**
 467 **of theoretical applicability, experimental studies have shown that the Kronig and Brink solution gives**
 468 **a reasonably good prediction of the mass transfer coefficient even at Reynolds numbers well above**
 469 **those corresponding to creeping flow.**^[108] Employing the average residence time of the metal droplets
 470 ($\overline{t_{md}}$) as the characteristic time, the Fourier number for mass transfer can be defined according to

$$Fo_M = \frac{4D_L \overline{t_{md}}}{d_{32,md}^2}. \quad (72)$$

472
 473 The corresponding Fourier number for heat transfer (Fo_H) is obtained from Eq. 72 by replacing mass
 474 diffusivity with thermal diffusivity. Thus the heat transfer coefficient for the metal droplets is
 475 obtained by replacing Sh and Fo_M with Nu and Fo_H , respectively. The mass transfer in the slag phase
 476 surrounding the metal droplets was calculated according to Eq. 73, which is valid for fluid spheres in
 477 creeping flow.^[109]

$$Sh = 0.65 \left(\frac{\mu_S}{\mu_S + \mu_L} \right)^{1/2} Re^{1/2} Sc^{1/2} \quad (73)$$

$$= 0.65 \left(\frac{\mu_S}{\mu_S + \mu_L} \right)^{1/2} \left(\frac{\rho_S \overline{u_{md}} d_{32,md}}{\mu_S} \right)^{1/2} \left(\frac{\mu_S}{\rho_S D_S} \right)^{1/2},$$

479
 480 where $\overline{u_{md}}$ is the average terminal velocity of the metal droplets in the emulsion. The heat transfer
 481 coefficient for the slag phase in contact with the metal droplets was obtained using the analogue of
 482 heat and mass transfer by replacing Sh and Sc with Nu and Pr , respectively.

483 **2.6 Thermodynamic properties**

484 All the thermodynamic properties were defined at the composition and temperature of the reaction
485 interface in question. The equilibrium constants are defined by

486

$$K = \exp\left(-\frac{\Delta G^\circ}{RT^*}\right) \text{ where } \Delta G^\circ = \Delta H^\circ - T^*\Delta S^\circ, \quad (74)$$

487

488 where R is the gas constant, T^* is the temperature of the reaction interface, and ΔG° , ΔH° and ΔS° are
489 the changes in Gibbs free energy, enthalpy and entropy of reaction, respectively. The reaction
490 enthalpy and reaction entropy were calculated according to Eqs. 75 and 76, respectively.

491

$$\Delta H^\circ = \sum_{i=1}^n \nu_i H_i^\circ, \quad (75)$$

$$\Delta S^\circ = \sum_{i=1}^n \nu_i S_i^\circ, \quad (76)$$

492

493 where ν_i , H_i° and S_i° are the stoichiometric coefficient, enthalpy and entropy of species i . The values
494 of H_i° and S_i° at temperature T were calculated as follows:

495

$$H^\circ(T) = H_{298.15}^\circ + \int_{298.15}^T C_p dT + H_{tr,T}^\circ + H_{dis}^\circ, \quad (77)$$

$$S^\circ(T) = S_{298.15}^\circ + \int_{298.15}^T \frac{C_p}{T} dT + S_{tr,T}^\circ + S_{dis}^\circ, \quad (78)$$

496

497 where $H_{298.15}^\circ$ is the enthalpy at 298.15 K (25 °C), C_p is the molar heat capacity, H_{tr}° is the total
498 enthalpy of phase transformations from 298.15 K (25 °C) to T , H_{dis}° is the enthalpy of dissolution,
499 $S_{298.15}^\circ$ is the entropy at 298.15 K (25 °C), S_{tr}° is the total entropy of phase transformations from
500 298.15 K (25 °C) to T , and S_{dis}° is the entropy of dissolution. The enthalpies H° and entropies S°
501 correspond to the following standard states: the Henrian standard state for the species dissolved in
502 the steel bath and the Raoultian standard state for the gas and slag species. For the dissolved species,
503 the relevant values of H_{dis}° and S_{dis}° were obtained from Sigworth and Elliott^[110], while for the gas
504 and slag species H_{dis}° and S_{dis}° were set to zero. The molar heat capacity at temperature T is solved
505 from the Shomate equation^[111].

506

$$C_p = A + B \cdot 10^{-3}T + C \cdot 10^5 T^{-2} + D \cdot 10^{-6} T^2, \quad (79)$$

507

508 where A , B , C and D are fitting parameters applicable to a certain temperature interval. A
 509 comprehensive database of the Shomate equation parameters was taken from HSC Chemistry^[111].
 510 The partial pressures of the gaseous species can be calculated from the ideal gas law based on the
 511 total gas pressure at the reaction interface. The Henrian activity coefficients of the species in the
 512 liquid metal phase were calculated with the Unified Interaction Parameter (UIP) formalism^[112]:

513

$$\ln \gamma_i^H = \ln \frac{\gamma_i^R}{\gamma_i^\circ} = -0.5 \sum_{j=1}^n \sum_{k=1}^n \varepsilon_j^k x_j^* x_k^* + \sum_{j=1}^n \varepsilon_i^j x_j^*, \quad (80)$$

514

515 where γ_i^H is the Henrian activity coefficient of species i , γ_i^R is the Raoultian activity coefficient of
 516 species i , γ_i° is the activity coefficient of species i at infinite dilution, ε is the first-order molar
 517 interaction parameter and x^* is the molar fraction at the reaction interface. The employed first-order
 518 molar interaction parameters are given in Table 2.

519

520 **Table 2** Refs. ^[113] ^[114] ^[115] ^[116] ^[110]

521

522 The activity coefficients of the slag species were calculated according to the model employed by Wei
 523 and Zhu^[21]. The Raoultian activity coefficients of FeO, Cr₂O₃, MnO and SiO₂ are given by Eqs. 81,
 524 82, 83 and 84, respectively.

525

$$\begin{aligned} \log_{10} \gamma_{\text{FeO}}^R &= \frac{\varepsilon_1}{T^*} (x_{\text{CaO}}^* + x_{\text{MgO}}^*) (x_{\text{SiO}_2}^* + 0.25x_{\text{AlO}_{1.5}}^*) \\ &+ \frac{\varepsilon_2}{T^*} x_{\text{MnO}}^* (x_{\text{SiO}_2}^* + 0.45x_{\text{CrO}_{1.5}}^*) + \frac{\varepsilon_3}{T^*} x_{\text{AlO}_{1.5}}^* x_{\text{SiO}_2}^* \end{aligned} \quad (81)$$

$$+ \frac{\varepsilon_4}{T^*} x_{\text{MnO}}^* x_{\text{AlO}_{1.5}}^* + \frac{\varepsilon_5}{T^*} x_{\text{CrO}_{1.5}}^* x_{\text{SiO}_2}^*,$$

$$\log_{10} \gamma_{\text{Cr}_2\text{O}_3}^R = \log_{10} \gamma_{\text{FeO}}^R - \frac{\varepsilon_6}{T^*} (x_{\text{CaO}}^* + x_{\text{MgO}}^*) - \frac{\varepsilon_7}{T^*} x_{\text{MnO}}^* - \frac{\varepsilon_5}{T^*} x_{\text{SiO}_2}^*, \quad (82)$$

$$\log_{10} \gamma_{\text{MnO}}^R = \log_{10} \gamma_{\text{FeO}}^R - \frac{\varepsilon_2}{T^*} (x_{\text{SiO}_2}^* + 0.45x_{\text{CrO}_{1.5}}^*) - \frac{\varepsilon_4}{T^*} x_{\text{AlO}_{1.5}}^*, \quad (83)$$

$$\log_{10} \gamma_{\text{SiO}_2}^R = \log_{10} \gamma_{\text{FeO}}^R - \frac{\varepsilon_1}{T^*} (x_{\text{CaO}}^* + x_{\text{MgO}}^*) - \frac{\varepsilon_2}{T^*} x_{\text{MnO}}^* \quad (84)$$

$$- \frac{\varepsilon_3}{T^*} x_{\text{AlO}_{1.5}}^* - \frac{\varepsilon_5}{T^*} x_{\text{CrO}_{1.5}}^*,$$

526

527 where $\varepsilon_1 \dots \varepsilon_7$ are the interaction coefficients of the model. Table 3 shows the interaction coefficients

528 reported by Wei and Zhu^[21] for early and later periods of refining. In this work, the coefficients
 529 applicable for the early period of refining were employed. Similar to Wei and Zhu,^[21] it was assumed
 530 that $a_{\text{Cr}_2\text{O}_3}^{\text{R}} = 1$ if the interfacial Cr_2O_3 content is greater than the maximum solubility of Cr_2O_3 in the
 531 slag.

532
 533 **Table 3** Ref. ^[21]

534 2.7 Physical properties

535 The physical properties of the steel and slag phases were estimated at the temperature of the reaction
 536 interface, while the properties of the gas phase were defined at gas film temperature, which was
 537 approximated as^[117]

$$T_{\text{G}} = 0.5 \times (T^* + T_{\text{jet}}), \quad (85)$$

538
 539 where T^* is the temperature of reaction interface and T_{jet} is the temperature of the gas jet. The
 540 effective mass diffusivity was defined for each species in the metal phase as the interdiffusivity in
 541 liquid iron, while only one effective diffusivity value was assigned for the gas and slag phases. Where
 542 possible, the temperature dependency of the mass diffusivity of solutes in liquid iron was described
 543 by an Arrhenius type relationship^[118]. In order to account for the effect of pressure and temperature,
 544 the mass diffusivity of the gaseous species was treated according to^[29]

$$D_{\text{G}} = D_{\text{G,eff}} \times \left(\frac{T_{\text{G}}}{T_{\text{ref}}}\right)^{1.5} \left(\frac{p_{\text{ref}}}{p_{\text{G}}}\right), \quad (86)$$

546
 547 where $D_{\text{G,eff}}$ is the effective mass diffusivity at T_{ref} and p_{ref} , T_{ref} is the reference temperature, p_{ref} is
 548 the reference pressure and p_{G} is the total gas pressure. The pressure changes in the gas jet are small
 549 enough to be neglected^[72] and hence the total gas pressure was taken as equal to the atmospheric
 550 pressure at both reaction interfaces. The treatment of other physical properties is summarized in **Table**
 551 **4** along with their corresponding references.

552
 553
 554 **Table 4** Refs. ^{[119] [120] [121] [122–124] [125] [126] [118] [127] [128] [119] [130] [129]}

555
 556
 557 During decarburization, the top slag consists of a molten slag phase saturated with chromium oxide
 558 and a solid chromium oxide phase.^[131] For this reason, it is necessary to consider the effect of solid

559 particles on the viscosity of the top slag. The viscosity of the liquid part ($\mu_{S(l)}$) was calculated using
 560 the viscosity model proposed by Forsbacka *et al.*^[125], which is an extension of the modified Urbain
 561 model^[132] for the $\text{Al}_2\text{O}_3\text{-CaO-CrO-Cr}_2\text{O}_3\text{-FeO-MgO-SiO}_2$ system. The effective viscosity of the top
 562 slag was determined as relative to the viscosity of the liquid slag phase:

$$\mu_s = \mu_{S(l)}\mu_{s,rel} \quad (87)$$

564
 565 The relative viscosity $\mu_{s,rel}$ was calculated according to the equation proposed by Thomas^[126]. **Figure**
 566 **5** provides a comparison of the Thomas^[126] equation with other relative viscosity equations available
 567 in the literature^[133–139]. With the exception of the Einstein equation^[133], the equations produce similar
 568 results up to a solid volume fraction of 0.3, but begin to diverge as the solid volume fraction
 569 approaches unity. The solid volume fraction was calculated as a function of Cr_2O_3 content as shown
 570 in the second part of this work^[44].

571

572 **Figure 5** Refs. ^[126,133–139]

573 2.8 Numerical solution

574 The objective of the numerical solution routine is to minimize the error in free variables, while
 575 minimizing the error in thermodynamic equilibrium at the reaction interfaces. The thermodynamic
 576 equilibrium at the reaction interface and the mass transfer onto and from the interface are solved
 577 simultaneously. However, conservation of mass and heat are solved successively. Using small time
 578 steps, this does not cause significant inaccuracy, but greatly improves the numerical stability. The
 579 flowchart of the model is shown in **Figure 6**.

580

581 **Figure 6**

582

583 The numerical solution of both iteration loops is obtained with Newton's method, which
 584 approximates the solution by its tangent line.^[140] For a set of non-linear equations the Newton's
 585 method can be expressed as follows:^[50]

586

$$\mathbf{J} \times \partial \mathbf{x} = -\mathbf{f} \quad (88)$$

587

588 where \mathbf{J} is the Jacobian matrix of the system with respect to all free variables, $\partial \mathbf{x}$ is the correction
 589 vector and \mathbf{f} is the residual vector, which approaches zero asymptotically during the iteration. The

590 system of linear equations defined by Eq. 88 is solved by Gauss–Jordan elimination. During iteration,
 591 the vector of free variables is updated similar to the relaxed Newton's method. The calculation
 592 procedure is repeated until the numerical error is sufficiently small or the maximum number of
 593 iterations is exceeded. The error in the residual vector \mathbf{f} is measured using the l^2 -norm, which is the
 594 Euclidian length of the correction vector:

$$\|\Delta\mathbf{x}\|_2 = \sqrt{\sum_i \Delta x_i^2}. \quad (89)$$

596 As stated earlier, one of the main assumptions of the model is that the reaction interfaces reach their
 597 mass-transfer constrained equilibrium composition at every instant. During the numerical solution,
 598 the interfacial composition asymptotically approaches the composition dictated by the equilibrium
 599 constants, provided that the forward reaction rate coefficients (k_f) are sufficiently large. In order to
 600 assess the fulfilment of the equilibrium assumption, the concept of *equilibrium number* is introduced:

$$E = \left| 1 - \frac{Q}{K} \right|, \quad (90)$$

602 where Q and K denote the reaction quotient and the equilibrium constant, respectively. The reaction
 603 quotient is defined as follows:

$$Q = \frac{\sum_p a_p^{v_p}}{\sum_r a_r^{v_r}}, \quad (91)$$

606 where p and r denote reaction products and reactants, respectively. By definition, $Q = K$ at
 607 equilibrium. Because $Q \rightarrow K$ as $k_f \rightarrow \infty$, it follows that $E \rightarrow 0$ as $k_f \rightarrow \infty$. Owing to these properties,
 608 the equilibrium number provides a practical measure of the relative fulfilment of the equilibrium
 609 assumption. As a preliminary setting the maximum allowed error was set to $E = 0.1\%$ for all the
 610 studied reactions. During numerical solution, the forward reaction rate coefficients are increased
 611 periodically until the equilibrium numbers of all the reactions are below the maximum allowed error.
 612 A typical calculation time per time step is in the order of few seconds using a desktop PC (3.4 GHz).

615 3 Conclusions

616 The objective of this work was to develop a fast numerical model for the reactions that occur during
 617 top-blowing in the AOD process. More specifically, the aim was to create a model that considers

618 reactions both between the top-blown gas and the steel bath and between metal droplets and top slag.
 619 Employing the categorization proposed by Ding *et al.*^[41], the model derived in this work can be
 620 classified as a *complex process mechanism model*, because it emphasizes the local thermodynamic
 621 equilibrium and local heat and mass transfer characteristics. In the second part of this work,^[44] the
 622 model is validated with heats from a full size AOD vessel. In the future, the combined top- and side-
 623 blowing stage of the AOD process can be simulated as a combination of the top-blowing model
 624 derived in this work and the side-blowing model proposed earlier by Järvinen *et al.*^[29].

625 **Acknowledgements**

626 **This research has been conducted within the framework of the DIMECC SIMP research program.**
 627 Outokumpu Stainless Oy, the Finnish Funding Agency for Technology and Innovation (TEKES), the
 628 Graduate School in Chemical Engineering (GSCE), the Academy of Finland (projects 258319 and
 629 26495), the Finnish Foundation for Technology Promotion, the Finnish Science Foundation for
 630 Economics and Technology, and the Tauno Tönning Foundation are gratefully acknowledged for
 631 funding this work. The first author thanks Professor Herbert Pfeifer for the possibility to conduct part
 632 of the research at RWTH Aachen University. In addition, Professor Rauf Hürman Eriç, Kevin
 633 Christmann and Tim Haas are acknowledged for their valuable comments on this manuscript.

634 **Nomenclature**

635 **Symbols**

636	a	Activity
637	A	Surface area [m ²]
638	A_i	Parameter of the Kronig-Brink solution
639	C_p	Molar heat capacity at constant pressure [J/(mol·K)]
640	c_p	Specific heat capacity at constant pressure [J/(kg·K)]
641	d_t	Nozzle throat diameter [m]
642	d_{limit}	Fineness parameter of the RRS distribution [m]
643	$d_{32,\text{md}}$	Sauter mean diameter of the metal droplets [m]
644	D	Diffusion coefficient [m ² /s]
645	f_i	Mass fraction of size class i at place of birth
646	\mathbf{f}	Residual vector
647	g	Standard gravity [m/s ²]
648	ΔG°	Change in standard Gibbs free energy of reaction [J/mol]
649	ΔG_{tot}	Change in total Gibbs free energy [J/mol]

650	h_{cav}	Depth of the cavity [m]
651	h_{lance}	Distance of the top lance from the surface of the steel bath [m]
652	H°	Standard enthalpy [J/mol]
653	ΔH°	Change in standard reaction enthalpy [J/mol]
654	\mathbf{J}	Jacobian matrix
655	J_{eff}	Droplet generation rate multiplication factor
656	k_f	Forward reaction rate coefficient
657	K	Equilibrium constant
658	L	Characteristic length [m]
659	m	Mass [kg]
660	\dot{m}_{md}	Metal droplet generation rate [kg/s]
661	$\dot{m}_{md,eff}$	Effective metal droplet generation rate [kg/s]
662	M	Molar mass [kg/mol]
663	n_{lance}	Number of exit ports in a nozzle
664	n	Distribution exponent of the RRS distribution
665	p	Partial pressure
666	p_{cav}	Arc length of the cavity [m]
667	p_{amb}	Ambient pressure [Pa]
668	p_0	Stagnation pressure at upstream part of the top lance [Pa]
669	r_{cav}	Top radius of the cavity [m]
670	R	Gas constant [J/(mol·K)]
671	R''	Reaction rate [kg/(m ² ·s)]
672	R^2	Correlation coefficient
673	RF	Cumulative weight-fraction
674	S°	Standard entropy [J/(mol·K)]
675	ΔS°	Change in standard reaction entropy [J/(mol·K)]
676	$t_{md,i}$	Residence time of metal droplet size class i [s]
677	\bar{t}_{md}	Average residence time of the metal droplets [s]
678	T	Temperature [K]
679	T^*	Interfacial temperature [K]
680	u_G	Critical gas velocity [m/s]
681	u_j	Axial velocity of the gas jet [m/s]
682	$u_{md,i}$	Terminal velocity of metal droplet size class i [m/s]
683	\bar{u}_{md}	Average terminal velocity of the metal droplets [m/s]

684	u_τ	Turbulent shear stress velocity [m/s]
685	\dot{V}_G	Volumetric gas flow rate [Nm ³ /s]
686	\dot{V}'_G	Modified volumetric gas flow rate [Nm ³ /s]
687	x	Molar fraction
688	X	Cation fraction
689	$\delta\mathbf{x}$	Correction vector
690	y	Mass fraction
691	y^*	Interfacial mass fraction
692	$\ \Delta\mathbf{x}\ _2$	l^2 -norm
693		
694	Greek symbols	
695	α	Heat transfer coefficient [W/(m ² K)]
696	α	Interaction energy between cations [J]
697	β	Mass transfer coefficient [m/s]
698	γ	Activity coefficient
699	γ°	Activity coefficient at infinite dilution
700	δ_N	Thickness of the diffusion boundary layer [m]
701	δ_{Pr}	Thickness of the thermal boundary layer [m]
702	ε	First order molar interaction parameter
703	η	Constant
704	$\bar{\eta}_H$	Average microkinetic efficiency of heat transfer
705	$\bar{\eta}_M$	Average microkinetic efficiency of mass transfer
706	θ	Inclination angle of each nozzle relative to lance axis [°]
707	κ	Constant
708	λ	Heat conductivity [W/(m·K)]
709	λ_i	Parameter of the Kronig-Brink solution
710	μ	Dynamic viscosity [Pa·s]
711	ν	Stoichiometric coefficient
712	$\bar{\nu}$	Mass-based stoichiometric coefficient
713	π	Mathematical constant
714	ρ	Density [kg/m ³]
715	σ	Surface tension [N/m]
716	ϕ	Volume fraction
717		

718	Dimensionless numbers	
719	E	Equilibrium number
720	FO _H	Fourier number for heat transfer
721	FO _M	Fourier number for mass transfer
722	\overline{Gr}	Mean Grashof number
723	Gr _H	Grashof number for heat transfer
724	Gr _M	Grashof number for mass transfer
725	N _B	Blowing number
726	N' _B	Modified blowing number
727	Nu	Nusselt number
728	Sc	Schmidt number
729	Sh	Sherwood number
730	Pr	Prandtl number
731	Re	Reynolds number
732		
733	Subscripts and superscripts	
734	cav	Cavity
735	bath	Steel bath
736	em	Gas-metal-slag emulsion
737	G	Gas phase
738	H	Henrian standard state
739	in	Gas flow into the system
740	jet	Gas jet
741	L	Liquid metal phase
742	md	Metal droplet
743	out	Gas flow out of the system
744	plume	Gas plume
745	R	Raoultian standard state
746	rel	Relative
747	S	Slag phase
748	STP	Standard temperature and pressure according to the DIN 1343 standard ^[49] :
749		273.15 K (0 °C) and 101325 Pa.
750	slag	Top slag
751	(l)	Liquid state

752 (s) Solid state

753

754 **Indices**

755 **i Size class**

756 i Species

757 n Number of species

758 r Number of reactions

759 ψ Phase

760 ω Reaction interface

761 **References**

762 [1] B. V. Patil, A. H. Chan and R. J. Choulet: *Refining of Stainless Steels*, pp. 715-741, In: R. J.
763 Fruehan: *The Making, Shaping and Treating of Steel*. 11th Edition Steel Making and Refining,
764 The AISE Steel Foundation, Pittsburgh, PA, USA, 1998.

765 [2] J.-H. Wei, J.-C. Ma, Y.-Y. Fan, N.-W. Yu, S.-L. Yang, S.-H. Xiang and D.-P. Zhu: *Ironmaking*
766 *Steelmaking*, 1999, vol. 26, pp. 363-371.

767 [3] P. Ternstedt, A. Tilliander, P. G. Jönsson and M. Iguchi: *ISIJ Int.*, 2010, vol. 50, pp. 663-667.

768 [4] J.-H. Wei, H.-L. Zhu, H.-B. Chi and H.-J. Wang: *ISIJ Int.*, 2010, vol. 50, pp. 26-34.

769 [5] J.-H. Wei, Y. He and G.-M. Shi: *Steel Res. Int.*, 2011, vol. 82, pp. 693-702.

770 [6] H. Gorges, W. Pulvermacher, W. Rubens and H.-A. Dierstein: *Stahl Eisen*, 1979, vol. 99, pp.
771 1310-1312.

772 [7] P. R. Scheller and F.-J. Wahlers: *ISIJ Int.*, 1996, vol. 36, pp. S69-S72.

773 [8] H.-L. Zhu, J.-H. Wei, G.-M. Shi, J.-H. Shu, Q.-Y. Jiang and H.-B. Chi: *Steel Res. Int.*, 2007, vol.
774 78, pp. 305-310.

775 [9] T. Watanabe and T. Tohge: *Tetsu-to-Hagané*, 1973, vol. 59, pp. 1224-1236.

776 [10] S. Asai and J. Szekely: *Metall. Trans.*, 1974, vol. 5, pp. 651-657.

777 [11] J. Szekely and S. Asai: *Metall. Trans.*, 1974, vol. 5, pp. 1573-1580.

778 [12] R. J. Fruehan: *Ironmaking Steelmaking*, 1976, vol. 3, pp. 153-158.

779 [13] T. Ohno and T. Nishida: *Tetsu-to-Hagané*, 1977, vol. 63, pp. 2094-2099.

780 [14] T. Deb Roy and D. G. C. Robertson: *Ironmaking Steelmaking*, 1978, vol. 5, pp. 198-206.

- 781 [15] T. Deb Roy, D. G. C. Robertson and J. C. C. Leach: *Ironmaking Steelmaking*, 1978, vol. 5, pp.
782 207-210.
- 783 [16] A. E. Semin, A. P. Pavlenko, T. Andzhum and E. A. Shuklina: *Steel USSR*, 1983, vol. 13, pp.
784 95-97.
- 785 [17] T. Tohge, Y. Fujita and T. Watanabe: Proceedings of the 4th Process Technology Conference,
786 Chicago, IL, USA, 1984, pp. 129-36.
- 787 [18] P. Sjöberg: *Some aspects on the scrap based production of stainless steels*, Doctoral thesis, Royal
788 Institute of Technology, Stockholm, Sweden, 1994.
- 789 [19] J. Reichel and J. Szekely: *Iron Steelmaker*, 1995, vol. 22, pp. 41-48.
- 790 [20] M. Görnerup and P. Sjöberg: *Ironmaking Steelmaking*, 1999, vol. 26, pp. 58-63.
- 791 [21] J.-H. Wei and D.-P. Zhu: *Metall. Mater. Trans. B*, 2002, vol. 33, pp. 111-119.
- 792 [22] J.-H. Wei and D.-P. Zhu: *Metall. Mater. Trans. B*, 2002, vol. 33, pp. 121-127.
- 793 [23] N. Kikuchi, K. Yamaguchi, Y. Kishimoto, S. Takeuchi and H. Nishikawa: *Tetsu-to-Hagané*,
794 2002, vol. 88, pp. 32-39.
- 795 [24] B. Deo and V. Srivastava: *Mater. Manuf. Process.*, 2003, vol. 18, pp. 401-108.
- 796 [25] B. Kleimt, R. Lichterbeck and C. Burkat: *Stahl Eisen*, 2007, vol. 127, pp. 35-41.
- 797 [26] G.-M. Shi, J.-H. Wei, H.-L. Zhu, J.-H. Shu, Q.-Y. Jiang and H.-B. Chi: *Steel Res. Int.*, 2007, vol.
798 78, pp. 311-317.
- 799 [27] M. Järvinen, A. Kärnä and T. Fabritius: *Steel Res. Int.*, 2009, vol. 80, pp. 429-436.
- 800 [28] J.-H. Wei, Y. Cao, H.-L. Zhu and H.-B. Chi: *ISIJ Int.*, 2011, vol. 51, pp. 365-374.
- 801 [29] M. P. Järvinen, S. Pisilä, A. Kärnä, T. Ikäheimonen, P. Kupari and T. Fabritius: *Steel Res. Int.*,
802 2011, vol. 82, pp. 638-649.
- 803 [30] S. E. Pisilä, M. P. Järvinen, A. Kärnä, T. Ikäheimonen, T. Fabritius and P. Kupari: *Steel Res.*
804 *Int.*, 2011, vol. 82, pp. 650-657.
- 805 [31] D. R. Swinbourne, T. S. Kho, B. Blanpain, S. Arnout and D. E. Langberg: *Miner. Process. Extr.*
806 *Metall.*, 2012, vol. 121, pp. 23-31.
- 807 [32] N. Å. I. Andersson, A. Tilliander, L. T. I. Jonsson and P. G. Jönsson: *Steel Res. Int.*, 2012, vol.
808 83, pp. 1039-1052.
- 809 [33] N. Å. I. Andersson, A. Tilliander, L. T. I. Jonsson and P. G. Jönsson: *Steel Res. Int.*, 2013, vol.
810 84, pp. 169-177.
- 811 [34] N. Å. I. Andersson, A. Tilliander, L. T. I. Jonsson and P. G. Jönsson: *Ironmaking Steelmaking*,
812 2013, vol. 40, pp. 390-397.

- 813 [35] N. Å. I. Andersson, A. Tilliander, L. T. I. Jonsson and P. G. Jönsson: *Ironmaking Steelmaking*,
814 2013, vol. 40, pp. 551-558.
- 815 [36] V.-V. Visuri, M. Järvinen, P. Sulasalmi, E.-P. Heikkinen, J. Savolainen and T. Fabritius: *ISIJ*
816 *Int.*, 2013, vol. 53, pp. 603-612.
- 817 [37] V.-V. Visuri, M. Järvinen, J. Savolainen, P. Sulasalmi, E.-P. Heikkinen and T. Fabritius: *ISIJ*
818 *Int.*, 2013, vol. 53, pp. 613-621.
- 819 [38] R. J. Fruehan: *Metall. Trans. B*, 1975, vol. 6, pp. 573-578.
- 820 [39] Y. Tang, T. Fabritius and J. Härkki: *Steel Res. Int.*, 2004, vol. 75, pp. 373-381.
- 821 [40] J. Riipi, T. Fabritius, E.-P. Heikkinen, P. Kupari and A. Kärnä: *ISIJ Int.*, 2009, vol. 49, pp. 1468-
822 1473.
- 823 [41] R. Ding, B. Blanpain, P. T. Jones and P. Wollants: *Metall. Mater. Trans. B*, 2000, vol. 31, pp.
824 197-206.
- 825 [42] Y. Uchida, N. Kikuchi, K. Yamaguchi, Y. Kishimoto, S. Takeuchi and H. Nishikawa:
826 Proceedings of the 2nd International Conference on Process Development in Iron and
827 Steelmaking, Luleå, Sweden, 2004, pp. 69-78.
- 828 [43] J.-H. Wei and Y. Li: *Steel Res. Int.*, 2015, vol. 86, pp. 189-211.
- 829 [44] V.-V. Visuri, M. Järvinen, A. Kärnä, E.-P. Heikkinen, P. Kupari and T. Fabritius: *A*
830 *Mathematical Model for Reactions during Top-Blowing in the AOD Process: Validation and*
831 *Results*, Process Metallurgy Research Unit, University of Oulu, unpublished research, 2016.
- 832 [45] M. Järvinen, V.-V. Visuri, S. Pisilä, A. Kärnä, P. Sulasalmi, E.-P. Heikkinen and T. Fabritius:
833 *Mater. Sci. Forum*, 2013, vol. 762, pp. 236-241.
- 834 [46] M. Järvinen, V.-V. Visuri, E.-P. Heikkinen, A. Kärnä, P. Sulasalmi, C. De Blasio and T.
835 Fabritius: *ISIJ Int.*, 2016, vol. 56, pp. 1543-1552.
- 836 [47] Z. Song: *Modeling of Gas flows in Steelmaking Decarburization Processes*, p. 60, Doctoral
837 thesis, Royal Institute of Technology, Stockholm, Sweden, 2013.
- 838 [48] Y. Tang, T. Fabritius and J. Härkki: *Appl. Math. Model.*, 2005, vol. 29, pp. 497-514.
- 839 [49] Deutsches Institut für Normung e.V.: *DIN 1343, Referenzzustand, Normzustand, Normvolumen;*
840 *Begriffe und Werte*, DIN1343, Referenzzustand, Normzustand, Normvolumen; Begriffe und
841 Werte, 1990.
- 842 [50] R. Taylor and R. Krishna: *Multicomponent Mass Transfer*, p. 126, John Wiley & Sons, Inc., New
843 York, NY, USA, 1993.
- 844 [51] R. I. L. Guthrie: *Engineering in Process Metallurgy*, p. 282, Clarendon Press, Oxford, United
845 Kingdom, 1989.
- 846 [52] B. Deo and R. Boom: *Fundamentals of Steelmaking Metallurgy*, p. 170/176, Prentice Hall
847 International, Hertfordshire, United Kingdom, 1993.

- 848 [53] H.-J. Odenthal, U. Falkenreck and J. Schlüter: Proceedings of the European Conference on
849 Computational Fluid Dynamics, Egmond aan Zee, The Netherlands, 2006, pp. 21.
- 850 [54] N. Molloy: *J. Iron Steel Inst.*, 1970, vol. 208, pp. 943-950.
- 851 [55] S. Sabah and G. Brooks: *ISIJ Int.*, 2014, vol. 54, pp. 836-844.
- 852 [56] X. Zhou, M. Ersson, L. Zhong, J. Yu and P. Jönsson: *Steel Res. Int.*, 2014, vol. 85, pp. 273-281.
- 853 [57] S. K. Sharma, J. W. Hlinka and D. W. Kern: *Iron Steelmaker*, 1977, vol. 24, pp. 7-18.
- 854 [58] D. Nakazono, K.-I. Abe, M. Nishida and K. Kurita: *ISIJ Int.*, 2004, vol. 44, pp. 91-99.
- 855 [59] F. R. Cheslak, J. A. Nicholls and M. Sichel: *J. Fluid Mech.*, 1969, vol. 36, pp. 55-63.
- 856 [60] S. N. Krivoshapko and V. N. Ivanov: *Encyclopedia of Analytical Surfaces*, p. 110, Springer
857 International Publishing, Cham, Switzerland, 2015.
- 858 [61] C. K. Lee, J. H. Neilson and A. Gilchrist: *Iron Steel Int.*, 1977, vol. 50, pp. 175-184.
- 859 [62] C. K. Lee, J. H. Neilson and A. Gilchrist: *Ironmaking Steelmaking*, 1977, vol. 4, pp. 329-337.
- 860 [63] S. C. Koria and K. W. Lange: *Steel Res.*, 1987, vol. 58, pp. 421-426.
- 861 [64] K. W. Lange and S. C. Koria: *Wechselwirkung zwischen Sauerstoffstrahl und Roheisenschmelze*
862 *beim Sauerstoffaufblasverfahren*, Publ. Wiss. Film. Techn. Wiss./Naturw., Ser. 8, Nr. 9, Institut
863 für den Wissenschaftlichen Film, Göttingen, Germany, 1983, Film D 1386.
- 864 [65] J.-H. Wei and L. Zeng: *Steel Res. Int.*, 2012, vol. 83, pp. 1053-1070.
- 865 [66] S. C. Koria: *Wechselwirkung zwischen einem Gasstrahl und flüssiger Metallschmelze*, p. 14,
866 Doctoral thesis, RWTH Aachen University, Aachen, Germany, 1981.
- 867 [67] Subagyo, G. A. Brooks, K. S. Coley and G. A. Irons: *ISIJ Int.*, 2003, vol. 43, pp. 983-989.
- 868 [68] E. Schürmann and K. Rosenbach: *Arch. Eisenhüttenwes.*, 1973, vol. 44, pp. 761-768.
- 869 [69] W. Rubens: *Untersuchung der Schlackenwege und des Verschleißes des feuerfesten*
870 *Ausmauerung bei modifizierten AOD-Verfahren zur Erzeugung rostfreier Stähle*, p. 45, Doctoral
871 thesis, Clausthal University of Technology, Clausthal-Zellerfeld, Germany, 1988.
- 872 [70] K. Koch, W. Münchberg, H. Zörcher and W. Rubens: *Stahl Eisen*, 1992, vol. 112, pp. 91-99.
- 873 [71] T. X. Zhu, K. S. Coley and G. A. Irons: *Metall. Mater. Trans. B*, 2012, vol. 43, pp. 751-757.
- 874 [72] E. T. Turkdogan: *Chem. Eng. Sci.*, 1966, vol. 21, pp. 1133-1144.
- 875 [73] N. Standish and Q. L. He: *ISIJ Int.*, 1989, vol. 29, pp. 455-461.
- 876 [74] I. Hahn: *Untersuchungen zum Verspritzen von Schmelze in sekundärmetallurgischen Anlagen*,
877 p. 1, Doctoral thesis, RWTH Aachen University, Aachen, Germany, 1999.

- 878 [75] A. Feiterna, D. Huin, F. Oeters, P.-V. Riboud and J.-L. Roth: *Steel Res.*, 2000, vol. 71, pp. 61-
879 69.
- 880 [76] Z. Han and L. Holappa: *ISIJ Int.*, 2003, vol. 43, pp. 292-297.
- 881 [77] Z. Han and L. Holappa: *ISIJ Int.*, 2003, vol. 43, pp. 1698-1704.
- 882 [78] S. C. Koria and K. W. Lange: *Ironmaking Steelmaking*, 1983, vol. 10, pp. 160-168.
- 883 [79] K.-Y. Lee, H.-G. Lee and P. C. Hayes: *ISIJ Int.*, 1998, vol. 38, pp. 1242-1247.
- 884 [80] H. W. Meyer, W. F. Porter, G. C. Smith and J. Szekely: *J. Met.*, 1968, vol. 20, pp. 35-42.
- 885 [81] G. Lindstrand, P. G. Jönsson and A. Tilliander: Proceedings of the ISIJ-VDEh-Jernkontoret Joint
886 Symposium, Osaka, Japan, 2013, pp. 106-13.
- 887 [82] A. Nordquist, A. Tilliander, K. Grönlund, G. Runnsjö and P. Jönsson: *Ironmaking Steelmaking*,
888 2009, vol. 36, pp. 421-431.
- 889 [83] W. Kleppe and F. Oeters: *Arch. Eisenhüttenwes.*, 1977, vol. 48, pp. 139-143.
- 890 [84] S. Sabah, M. Alam, G. Brooks and J. Naser: 4th International Conference on Process
891 Development in Iron and Steelmaking, Luleå, Sweden, 2012, pp. 125-34.
- 892 [85] S. Sabah and G. Brooks: *Metall. Mater. Trans. B*, 2015, vol. 46, pp. 863-872.
- 893 [86] M. Alam, G. Irons, G. Brooks, A. Fontana and J. Naser: *ISIJ Int.*, 2011, vol. 51, pp. 1439-1447.
- 894 [87] S. Sarkar, P. Gupta, S. Basu and N. B. Ballal: *Metall. Mater. Trans. B*, 2015, vol. 46, pp. 961-
895 976.
- 896 [88] B. K. Rout, G. Brooks, Subagyo, M. A. Rhamdhani and Z. Li: *Metall. Mater. Trans. B*, 2016,
897 vol. 47, pp. 3350-3361.
- 898 [89] S. C. Koria and K. W. Lange: *Metall. Trans. B*, 1984, vol. 15, pp. 109-116.
- 899 [90] C. Cicutti, M. Valdez, T. Pérez, J. Petroni, A. Gómez, R. Donayo and L. Ferro: Proceedings of
900 the 6th International Conference on Motel Slags, Fluxes and Salts, Stockholm, Sweden - Helsinki,
901 Finland, 2000, pp. 1-17.
- 902 [91] S. C. Koria and K. W. Lange: *Ironmaking Steelmaking*, 1986, vol. 13, pp. 236-240.
- 903 [92] S.-Y. Kitamura and K. Okohira: *Tetsu-to-Hagané*, 1990, vol. 76, pp. 199-206.
- 904 [93] B. Deo, A. Karamcheti, A. Paul, P. Singh and R. P. Chhabra: *ISIJ Int.*, 1996, vol. 36, pp. 658-
905 666.
- 906 [94] Q. L. He and N. Standish: *ISIJ Int.*, 1990, vol. 30, pp. 356-361.
- 907 [95] G. Brooks, Y. Pan, Subagyo and K. Coley: *Metall. Mater. Trans. B*, 2005, vol. 36, pp. 525-535.
- 908 [96] R. C. Urquhart and W. G. Davenport: *Can. Metall. Q.*, 1973, vol. 12, pp. 507-516.

- 909 [97] Subagyo and G. A. Brooks: *ISIJ Int.*, 2002, vol. 42, pp. 1182-1184.
- 910 [98] H. Gou, G. A. Irons and W.-K. Lu: *Metall. Mater. Trans. B*, 1996, vol. 27, pp. 195-201.
- 911 [99] F. Oeters: *Metallurgie der Stahlherstellung*, p. 162/174/337, Verlag Stahleisen mbH, Düsseldorf,
912 Germany, 1989.
- 913 [100] H. Lohe: *Fortschr. -Ber. VDI-Z.*, 1967, Reihe 3, Nr. 15, pp. 1-59.
- 914 [101] N. Dogan, G. A. Brooks and M. A. Rhamdhani: *ISIJ Int.*, 2011, vol. 51, pp. 1102-1109.
- 915 [102] F. Memoli, C. Mapelli, P. Ravanelli and M. Corbella: *ISIJ Int.*, 2004, vol. 44, pp. 1342-1349.
- 916 [103] R. L. Steinberger and R. E. Treybal: *AIChE Journal*, 1960, vol. 6, pp. 227-232.
- 917 [104] K. W. Lange: *Arch. Eisenhüttenwes.*, 1971, vol. 42, pp. 233-241.
- 918 [105] R. Kronig and J. C. Brink: *Appl. Sci. Res.*, 1951, vol. 2, pp. 142-154.
- 919 [106] D. Colombet, D. Legendre, A. Cockx and P. Guiraud: *Int. J. Heat Mass Tran.*, 2013, vol. 67,
920 pp. 1096-1105.
- 921 [107] P. M. Heertjes, W. A. Holve and H. Talsma: *Chem. Eng. Sci.*, 1954, vol. 3, pp. 122-142.
- 922 [108] R. Clift, J. R. Grace and M. E. Weber: *Bubbles, drops and particles*, Academic Press, New
923 York, USA, 1978.
- 924 [109] P. H. Calderbank: *Chem. Engr.*, 1967, vol. 45, pp. 209-233.
- 925 [110] G. K. Sigworth and J. F. Elliott: *Met. Sci.*, 1974, vol. 8, pp. 298-310.
- 926 [111] Outotec Oyj: *HSC Chemistry* 8, 2015.
- 927 [112] A. D. Pelton and C. W. Bale: *Metall. Trans. A*, 1986, vol. 17, pp. 1211-1215.
- 928 [113] A. V. Alpatov and S. N. Paderin: *Russ. Metall.*, 2010, vol. 2010, pp. 557-564.
- 929 [114] W. E. Slye and R. J. Fruehan: *Proceedings of the 57th Electric Furnace Conference*, Pittsburgh,
930 PA, USA, 1999, pp. 401-12.
- 931 [115] S. Ueno, Y. Waseda, T. Jacob K. and S. Tamaki: *Steel Res.*, 1988, vol. 59, pp. 474-483.
- 932 [116] K. V. Malyutin and S. N. Paderin: *Russ. Metall.*, 2007, vol. 2007, pp. 545-551.
- 933 [117] J. Szekely and N. J. Themelis: *Rate Phenomena in Process Metallurgy*, p. 459, John Wiley &
934 Sons, Inc., New York, NY, USA, 1971.
- 935 [118] K. Nagata, Y. Ono, T. Ejima and T. Yamamura: *Diffusion*, pp. 181-204, In: Y. Kawai and Y.
936 Shiraishi: *Handbook of Physico-chemical Properties at High Temperatures*, The Iron and Steel
937 Institute of Japan, Tokyo, Japan, 1988.

- 938 [119] IAEA: *Thermophysical Properties of Materials for Nuclear Engineering: A Tutorial and*
939 *Collection of Data*, p. 169, International Atomic Energy Agency, Vienna, Austria, 2008.
- 940 [120] B. J. Keene and K. C. Mills: *Densities of molten slags*, pp. 313-348, In: Verein Deutscher
941 Eisenhüttenleute: *Slag Atlas 2nd Edition*, Verlag Stahleisen GmbH, Düsseldorf, Germany, 1995.
- 942 [121] C. R. Wilke: *J. Chem. Phys.*, 1950, vol. 18, pp. 517-519.
- 943 [122] R. B. Bird, W. E. Stewart and E. N. Lightfoot: *Transport Phenomena*, p. 23, John Wiley &
944 Sons, Inc., Singapore, 1960.
- 945 [123] G. H. Geiger and D. R. Poirier: *Transport phenomena in metallurgy*, p. 11, Addison-Wesley
946 Publishing Company, Reading, MA, USA, 1973.
- 947 [124] L. D. Cloutman: *A Database of Selected Transport Coefficients for Combustion Studies*, p. 5,
948 Lawrence Livermore National Laboratory, Livermore, CA, USA, 1993.
- 949 [125] L. Forsbacka, L. Holappa, A. Kondratiev and E. Jak: *Steel Res. Int.*, 2007, vol. 78, pp. 676-684.
- 950 [126] D. G. Thomas: *J. Colloid Sci.*, 1965, vol. 20, pp. 267-277.
- 951 [127] C. R. Wilke and C. Y. Lee: *Ind. Eng. Chem.*, 1955, vol. 47, pp. 1253-1257.
- 952 [128] K. C. Mills: *Diffusion coefficients in molten slags*, pp. 541-556, In: Verein Deutscher
953 Eisenhüttenleute: *Slag Atlas 2nd Edition*, Verlag Stahleisen GmbH, Düsseldorf, Germany, 1995.
- 954 [129] C. F. Wuppermann: *Mathematische Modellierung der fluidinduzierten Behälterschwingung*
955 *beim AOD-Prozess*, p. 58, Doctoral thesis, RWTH Aachen University, Aachen, Germany, 2013.
- 956 [130] Outotec Research Oy: *HSC Chemistry 7*, 1974-2009.
- 957 [131] O. Wijk: *Stainless Steelmaking in Converters*, pp. 280-301, In: T. A. Engh: *Principles of Metal*
958 *Refining*, Oxford University Press, Oxford, United Kingdom, 1992.
- 959 [132] G. Urbain: *Steel Res.*, 1987, vol. 58, pp. 111-116.
- 960 [133] A. Einstein: *Ann. Phys.*, 1906, vol. 19, pp. 289-306.
- 961 [134] E. Guth and R. Simha: *Kolloid Z.*, 1936, vol. 74, pp. 266-275.
- 962 [135] E. Guth: *J. Appl. Phys.*, 1945, vol. 16, pp. 20-25.
- 963 [136] H. M. Smallwood: *J. Appl. Phys.*, 1944, vol. 15, pp. 758-766.
- 964 [137] H. C. Brinkman: *J. Chem. Phys.*, 1952, vol. 20, pp. 571.
- 965 [138] J. Happel: *J. Appl. Phys.*, 1957, vol. 28, pp. 1288-1292.
- 966 [139] T. Kitano, T. Kataoka and T. Shirota: *Rheol. Acta*, 1981, vol. 20, pp. 207-209.
- 967 [140] E. Kreyszig, H. Kreyszig and E. J. Norminton: *Advanced Engineering Mathematics Tenth*
968 *Edition*, p. 909, John Wiley & Sons, Inc., Hoboken, NJ, USA, 2011.

970 **List of tables**

971 **Table 1.** Equations for calculating the geometry of the cavity.^[63]

972 **Table 2.** Employed first-order molar interaction parameters in liquid iron at 1873 K (1600°C).

973 **Table 3.** Interaction coefficients of the slag model.^[21]

974 **Table 4.** Employed models and parameters for physical properties.

975 **List of figures**

976 **Figure 1.** Schematic illustration of combined-blowing in an AOD vessel.

977 **Figure 2.** Schematic illustration of the interaction of the reaction interfaces.

978 **Figure 3.** Schematic illustration of the gas jet impact area with a one-hole lance.

979 **Figure 4.** Schematic illustration of the gas jet impact area with a 3-hole lance with non-coalescing
980 (A) and coalescing (B) cavities.

981 **Figure 5.** Calculated relative viscosity as a function of the volume fraction of solids^[126,133–139].

982 **Figure 6.** Flowchart of the reaction model.

983